Methodology for the Classification of Types of Land Use in the Metropolitan Area of the Valley of Mexico based on the Spectral Signature of Satellite Images and its Effect on the Rainfall Simulation with the WRF Model

Indalecio Mendoza Uribe, Víctor Kevin Contreras Tereza,
Pamela Iskra Mejía Estrada, Olivia Rodríguez López

Instituto Mexicano de Tecnología del Agua,
Subcoordinación de Hidrometeorología, Jiutepec,
Mexico

{indalecio_mendoza, victor_contreras, iskra_mejia, olivia_rodriguez}@tlaloc.imta.mx

Abstract. In numerical models of the atmosphere, data on land use are considered as initialization data, therefore a current classification at the simulation date will allow the model an appropriate representation of the processes related to the radiation balance and the hydrological cycle of the study area. In the particular case of the Weather Research and Forecasting model, the default database uses a classification of 21 categories of land use type, based on MODIS satellite images between the years 2001-2005 with a spatial resolution of 500 meters, therefore these data are not considered current or applicable to recent events. This paper proposes a methodology to update the classification of types of land use in the Metropolitan Area of the Valley of Mexico based on the analysis of the spectral signature of Landsat 8 satellite images and derived indices, as well as the statistical validation of its effect in the numerical simulation of rainfall with the WRF model.

Keywords. Scientific computing, remote sensing, weather forecasting, model validation, urban areas.

1 Introduction

Numerical models of the atmosphere, based on initial meteorological data, apply physical-mathematical models to calculate the future state of meteorological variables such as relative humidity, temperature, precipitation, wind speed and direction, among others. With the advancement of computing and knowledge of the atmosphere, these models have evolved and correspond to the first consultation reference in operational forecasting centers. Among the input data, the models consider the geographical characteristics of the study area, among which are the topography, Coriolis force, angle of rotation of the earth and definition of type of land use. The latter allows an appropriate representation of processes related to the radiation balance and the local hydrological cycle [8].

The WRF (Weather Research and Forecasting) model has become the most widely used in the scientific community with more than 57,800 users from 160 countries [23]. This model was developed by different institutions in the US, including NCAR (National Center for Atmospheric Research), NCEP (National Centers for Environmental Prediction) and NOAA (National Oceanic and Atmospheric Administration). The main characteristics of the model revolve around its non-hydrostatic dynamics and its ability to operate in spatial resolutions of a few kilometers.

Contains different configuration options and physical parameterizations for convection, microphysics, planetary boundary layer, radiation, among other hydrothermodynamic processes.

The model code is open to the community and has been optimized for operation in both shared and distributed memory computing environments [3, 30].

The WRF model uses by default a classification of 21 categories of land use type, defined in the International Geosphere and Biosphere Program (IGBP), based on MODIS satellite images between

2001-2005 and a resolution of 500 meters [7]. However, over the years, naturally or by anthropogenic effect, there are changes in the type of land use in specific areas, for example, the transfer of grasslands and scrublands to agricultural uses [33], so the default database is not considered current or applicable to recent events or several years prior to its creation.

On the other hand, remote sensing is fundamentally based on the fact of working with descriptive information of phenomena and objects present in the physical universe that has been collected without coming into contact with them, making it a very efficient alternative for remote monitoring [17]. Remote sensing makes it possible to explore various aspects of our planet in different spectral bands.

For example, through remote sensing it is possible to identify changes in vegetation cover and bodies of water, types of climates, advance or retreat of glaciers, felling of forests, erosion processes, among others [20, 34]. In addition to the direct use of the different spectral bands, derived spectral indices have been developed, which allow to improve the identification of characteristics or objects that are not directly identifiable from the satellite bands [1, 10,29].

The objective of this work was to apply a methodology for the classification of types of land use in the Metropolitan Zone of the Valley of Mexico based on the analysis of the spectral signature of Landsat 8 Satellite images and derived indices to later replace the default database of the WRF model and statistically evaluate its effect on the precipitation simulation for a selected event with extraordinary rainfall in the year 2020.

2 Metodology

2.1 Study Zone

The Metropolitan Zone of the Valley of Mexico (ZMVM or Valley of Mexico) is located at 19°20' North Latitude and 99°05' West Longitude, in the center of the country, forming part of a basin, which has an average elevation of 2,240 meters above sea level (masl); it presents intermountain valleys, plateaus and ravines, as well as semi-flat terrain,

in what were once the lakes of Chalco, Texcoco and Xochimilco [30]. The ZMVM is the main economic, financial, political and cultural center of Mexico. With respect to its population, it is the third largest metropolitan area in the Organization for Economic Cooperation and Development (OECD) and the largest in the world outside of Asia. According to the most used Mexican delimitations, the ZMVM covers around 9,560 km^2 (almost five times the size of the Greater London region and three times that of Luxem-bourg), includes the 16 delegations of the Federal District, 59 municipalities of the state of Mexico and one municipality of the state of Hidalgo [26].

2.2 Datasets

2.2.1 Meteorological Fields

To generate the initial and boundary conditions required by the WRF model, data from the Global Tropospheric Analysis System of the NCEP FNL (Final) operational model were used, which operates from the month of July 1999 [24]. The FNL data was downloaded from the 7th at 00:00 until the 9th of June at 18:00 of the year 2020, in UTC time (Universal Time Coordinated). These data are in GRIB format with a temporal resolution of 3 hours and a spatial resolution of 27 km.

2.2.2 LANDSAT Satellite Images

For the analysis of the spectral signature, the images of the Landsat 8 satellite, launched into space in August 2012, were used. Contains 11 bands with an average resolution of 30 m, which allows a wide range of applications. The consultation, download and cropping of the images was carried out by means of Google Earth Engine (GEE), tool developed by the company Google that allows geospatial analysis to be carried out using processing and data collections in the cloud [27].

Using GEE's Javascript code editor, the process of selecting, cutting and downloading the images for the ZMVM in Tiff format was automated. Four images were selected for the year 2020, one per season of the year, applying as the main criterion the selection of images without the presence of clouds that could affect the classification. The values of the 11 bands were normalized on a scale of 0 to 1.
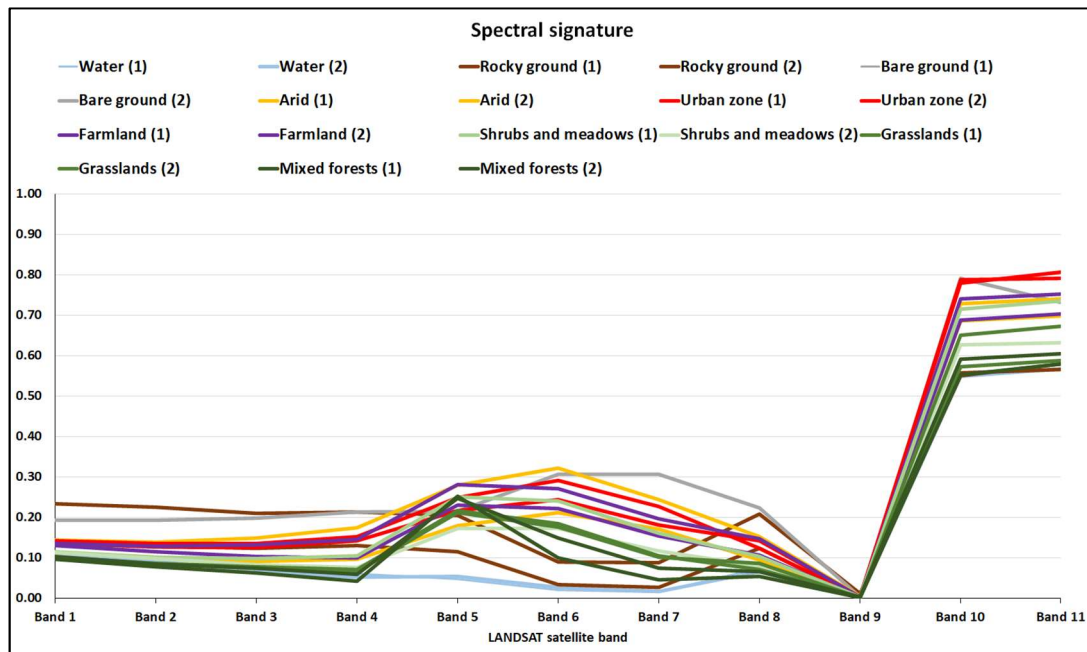
Fig. 1. Spectral signature per band

2.2.3 Rainfall Records

As observed data, the daily rainfall records of the weather stations of the Hydrological Information System (SIH) were used, operated by the Surface Water and River Engineering Management (GASIR) of the National Water Commission (CONAGUA). The data from these stations correspond to the accumulated rainfall from 6:00 hours of the day before to 6:00 hours of the day of registration.

For this study, only the data reported for June 9, 2020 was used, being a total of 82 weather stations that contained data in the study area. The maximum precipitation reported for this date was 63.5 mm at the station "Las arboledas" with ARBMX station key, latitude 19.5667, longitude -99.2167 and an elevation of 2,280 masl.

2.3 Analysis of the Spectral Signature

The analysis of the spectral signature and derived indices was carried out to identify 10 types of land use: arid soil, bare ground, farmland, grasslands, snow, mixed forests, rocky ground,

shrubs/meadows, urban zone and water. The selected spectral indices are described below.

The Normalized Difference Building Index (NDBI), allows estimating built-up surfaces or construction development [4, 35]. It is expressed in values from -1 to 1. Positive values indicate areas built up or under construction, while negative values indicate areas with vegetation or bare soil (Eq. 1):

$$NDBI = \frac{SWIR - NIR}{SWIR + NIR}, \tag{1}$$

where NIR correspond to near infrared (band 5 on Landsat 8) and SWIR correspond to shortwave infrared (band 6 on Landsat 8).

The Normalized Difference Vegetation Index (NDVI), identifies presence of vegetation [29]. It is expressed in values from -1 to 1 (Eq. 2). Values greater than 0.2 indicate areas with vegetation, while opposite values indicate urban areas, arid soils, among others:

$$NDVI = \frac{NIR - Red}{NIR + Red}, \tag{2}$$

where Red corresponde to visible red (band 4 on Landsat 8) and NIR correspond to near infrared (band 5 on Landsat 8).
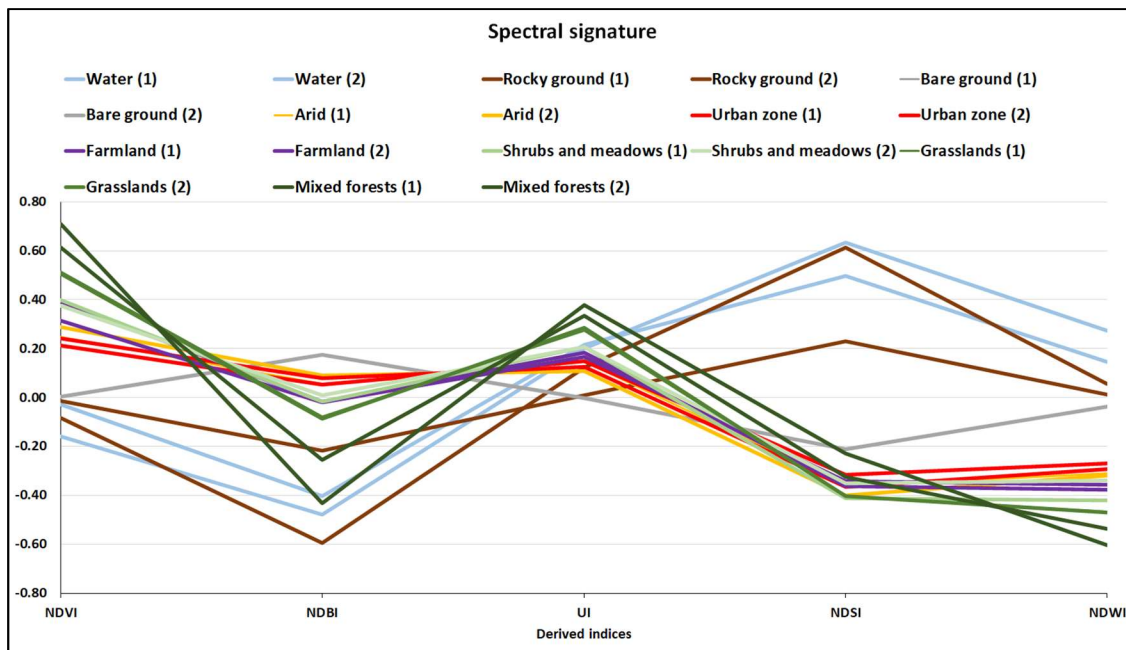
Fig. 2. Spectral signature by derived index2.4 LANDSAT classification

The Urban Index (UI), allows estimation of built-up areas [14]. It is expressed in values from -1 to 1. Where positive values indicate urbanized areas, while negative values refer to bare or vegetated areas (Eq. 3):

$$UI = \frac{SWIR-VNIR}{SWIR+VNIR}, \qquad (3)$$

where SWIR correspond to shortwave infrared 1 (band 6 on Landsat 8) and VNIR correspond to shortwave infrared 2 (band 7 on Landsat 8).

The Normalized Difference Snow Index (NDSI). It is expressed in values from -1 to 1. Where values close to 1 indicate areas with ice or snow (Eq. 4):

$$NDSI = \frac{Green-SWIR}{Green+SWIR}, \qquad (4)$$

where Green correspond to visible green (band 3 on Landsat 8) and SWIR correspond to shortwave infrared 1 (band 6 on Landsat 8).

The Normalized Differential Water Index (NDWI), allows to identify water masses and areas saturated with moisture [5]. It is expressed in values between -1 and 1. Positive values indicate bodies of water, flooded or humid areas, while negative values indicate dry areas (Eq. 5):

$$NDWI = \frac{Green-NIR}{Green+NIR}, \qquad (5)$$

where Green correspond to visible green (band 3 on Landsat 8) and NIR correspond to near infrared (band 5 on Landsat 8).

Subsequently, the spectral signatures were generated for two points, randomly selected, for the types of land use defined, with the exception of the snow category because no pixels were found in the treated images.

Significant variations were observed during the year in the categories of vegetation cover and bodies of water; therefore, it was determined to make an average of the images corresponding to the four seasons of the year, determining the spectral signature on these values.

Figures 1 and 2 present the spectral signature by type of land use by band and by spectral index respectively.

Based on the bibliography and on the analysis of both the spectral signature and the derived indices, it was possible to define a classification of 10 categories of land use types called LANDSAT classification.

Table 1. Land use type categories identified based on the spectral signature and indices derived from the LANDSAT satellite

Index	Land use	NDVI value	Other values
1	Water bodies		NDWI >= 0.1
2	Snow	<= 0.0	NDSI >= 0.9
3	Rocky ground		
4	Bare ground	<= 0.10	
5	Arid soil		
6	Urban zone	<= 0.25	Band 10 >= 0.75 Band 11 >= 0.75 UI >= 0.05 NDBI >= 0.05
7	Farmland	<= 0.4	Band 1 >= 0.1225 Band 2 >= 0.1069
8	Shrubs and meadows		
9	Grasslands	<= 0.6	
10	Mixed forest	> 0.6	

Table 2. Equivalence between land use type indices between the default database of the WRF model (MODIS) and the LANDSAT classification

MODIS		LANDSAT	
Index	Land use	Index	Land use
1	Evergreen needle-leaf forest		
2	Evergreen broadleaf forest		
3	Deciduous Needle-Leaf Forest	10	Mixed forest
4	Deciduous forest		
5	Mixed forest		
6	Closed scrub		
7	Open scrub	8	Shrubs and meadows
8	Wooded savannahs		
9	Savannahs		
10	Grasslands	9	Grasslands
11	Permanent wetlands	1	Water bodies
12	Farmland	7	Farmland
13	Urban and build	6	Urban zone
14	Mosaic of farmland / natural vegetation	7	Farmland
15	Ice/Snow	2	Snow
16	Barren or sparsely vegetated	3	Rocky ground
		4	Bare ground
		5	Arid soil
17	Water	1	Water bodies
18	Wooded tundra	[Unclassified]	
19	Mixed tundre	[Unclassified]	
20	Barren tundre	[Unclassified]	
21	Lakes	1	Water bodies

The NDVI allowed a clear distinction to be made between the categories with vegetation from the rest, therefore it was determined that this index can be used as the first classification filter, but not determining, since some types of soil, such as arid soil, farmland and urban areas presented values in the same range.

For these categories, the values of other indices and specific bands are considered. Table 1 presents the LANDSAT classification and the key values for its detection.

Subsequently, a relationship was created between the 21 categories of land use type that the WRF model uses by default (MODIS), and the 10 categories of the LANDSAT classification obtained from the previous analysis. Table 2 shows the LANDSAT classification indices and their equivalence in MODIS.

The steps to generate the LANDSAT classification are as follows:

Step 1. Open Geotiff file with the 11 bands of the LANDSAT satellite.

Step 2. Read the 11 bands into independent variables.

Step 3. Calculate the derived indices NDBI, NDVI, NDSI AND NDWI and UI.

Step 4. Obtain dimensions nx and ny of the satellite bands.

Step 5. Create the classification array of ny and nx dimensions.

Step 6. Iterate for each mesh point and assign the category to the variable classification according to the values of the table 1.

Step 7. Close Geotiff file.

The classification variable will be used in the process of updating the LU_INDEX variable of the file with the default geographic data of the WRF model.

It is necessary to point out that, for each category, here are values corresponding to the physical parameters of albedo, soil moisture availability, surface emissivity, roughness thickness, thermal inertia and surface heat capacity that considers the WRF model for each type of specific land use, these values are found in the LANDUSE.TBL file, included within the model file structure.

2.5 Updating the Land Use Type Layer

Once the LANDSAT classification has been obtained, with 30 m resolution, the values of the LU_INDEX variable of the original file were updated with the geographic data of the d02 domain (geo_em.d02) generated with the WPS (WRF Preprocessing System) module, the latter with a resolution of 1 km.

This process involves sampling all the points of the LANDSAT classification contained for each grid point of the variable LU_INDEX and assigning it the modal value. The WRF model uses an Arakawa-C type mesh [31], therefore, each grid point has geographic coordinates that correspond to the center (XLAT_M and XLONG_M), to the vertex V (XLAT_V and XLONG_V) and to the vertex U (XLAT_U and XLONG_U).

The steps for updating the LU_INDEX variable with the LANDSAT classification are as follows:

Step 1. Open the file with the geographic data (by default) of the domain d02 in NetCDF format (geo_em.d02), which were generated by the WPS module.

Step 2. Read the variables LU_INDEX, XLAT_U, XLONG_U, XLAT_V and XLONG_V.

Step 3. Get ny and nx dimensions of the variable LU_INDEX.

Step 4. Iterate y and x for each mesh point and update LU_INDEX according to the following:

Step 4.1. Obtain minimum longitude (lonMin) of vertex U (XLONG_U[y, x])

Step 4.2. Get maximum longitude (LongMax) of vertex U (XLONG_U[y, x+1])

Step 4.3. Get minimum latitude (latMin) of vertex V (XLAT_V[y, x])

Step 4.4. Get maximum latitude (latMax) of vertex V (XLAT_V[y+1, x])

Step 4.5. Find the indices iy1 and iy2 in the LANDSAT classification mesh within the vertices of the LU_INDEX cell corresponding to latMin and latMax.

Step 4.6. Find the indices ix1 and ix2 in the LANDSAT classification grid within the vertices of the LU_INDEX cell corresponding to lonMin and lonMax.

Step 4.7. Extract from the classification variable a subgrid of the segment [iy2:iy1,ix1:ix2] and store it in the tmp variable.

Step 4.8. Get the mode of the variable tmp.

Table 3. Configuration parameters of the domains of the WRF model

Parameter	Description	Parent domain (d01)	Nested domain (d02)
i_parent_start	Starting Lower Left Corner I-indices from the parent domain	1	27
j_parent_start	Starting Lower Left Corner J-indices from the parent domain	1	27
e_we	End index in x (west-east) direction	51	86
e_sn	End index in y (south-north) direction	51	86
dx/dy	Grid length in x/y direction, unit in meters	5000	1000
Parent_grid_ratio	Parent-to-nest domain grid size ratio.	1	5
Lat_central	Real value with the central latitude of the parent domain.	20.687	Does not apply
Long_central	Real value with the central longitude of the parent domain.	-103.348	Does not apply

Table 4. Selected parameterization schemes in the WRF model

Process	Parameterization scheme (for both domains)
Microphysics	Option 9: Milbrandt–Yau Double Moment Scheme [15, 16].
Convection	Option 3: Grell–Freitas Ensemble Scheme [9].
Planetary boundary layer	Option 5: Mellor–Yamada Nakanishi Niino Level 2.5/3 Schemes [21, 22, 25].
Layer options surface	Option 1: Revised MM5 Scheme [13].
Land surface options	Option 1: 5–layer Thermal Diffusion Scheme [6].
Long wave radiation	Option 4: RRTMG Longwave Scheme [11].
Short wave radiation	Option 4: RRTMG Shortwave Scheme [11].
Urban surface options	Option 1: Single Layer Urban Canopy Model [4]

Step 4.9. Replace LU_INDEX[y,x] with mode.

Step 5. Update the LU_INDEX variable in the file with the geographic data.

Step 6. Close the Geo file.

2.6 Rainfall Simulation with the WRF Model

For this study, the ARW (Advanced Research WRF) kernel was used in its version 4.2. This kernel allows horizontal nesting, making it possible to obtain a higher resolution in a specific area, this is achieved by adding one or more additional meshes or domains to the simulation. This option is for horizontal refinement, with rectangular meshes that are aligned to a coarser parent mesh called the parent domain (d01), within which subsequent meshes can be nested (d02, d03, etc.) called nested domains [18].

Among the good practices, it is recommended to scale down between the parent and nested domains from 1-3 or 1-5 to maintain stability in the model. For the simulation of rainfall in the ZMVM,

the WRF model was configured for domains d01 and d02 with 5 and 1 km resolution, respectively, thus maintaining the relation 1-5.

Two numerical simulations were carried out to obtain the accumulated rainfall in 24 hours between June 8 at 6:00 hours and June 9 at 6:00 hours, same period of the observed data selected from the SIH database.

Simulations were performed with a 38 hours warm-up, the first using the MODIS default land use type and the second with the LANDSAT classification.

Although exact methods exist to solve small-scale physical processes, these are not considered appropriate for their application in numerical models because they require a long computation time and the meteorological values required for their calculation are not included in the required scale and quality.

So that, the WRF model uses different types of parameterizations to simplify processes that are too small and complex. Table 3 shows the main
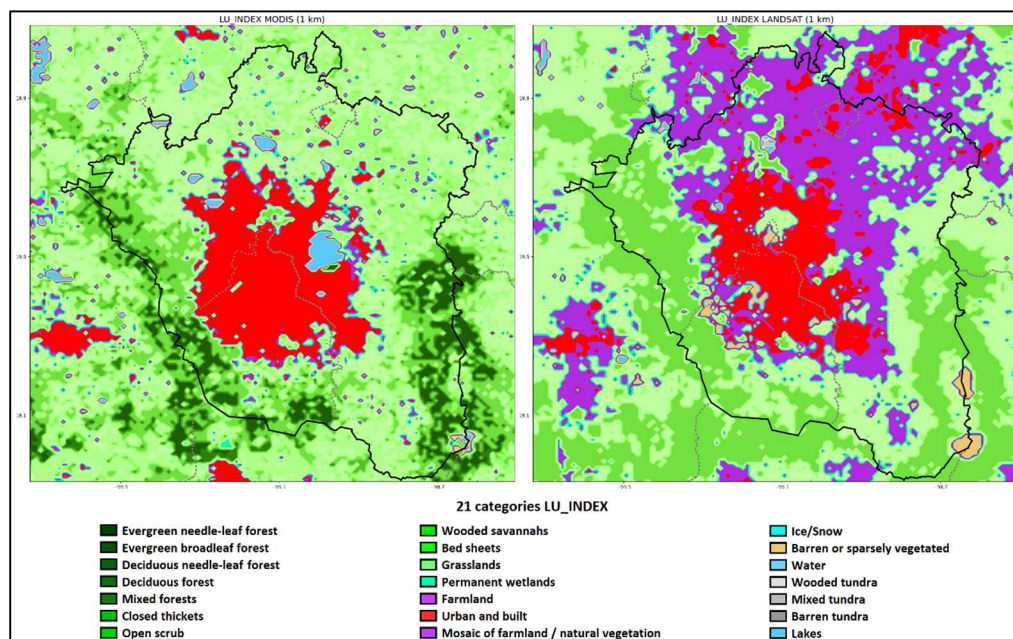
Fig. 3. MODIS classification (left) and LANDSAT classification (right)

configuration parameters of the domains. Table 4 shows the parameterization schemes selected for this study.

2.7 Statistical Evaluation

To measure the effect of updating the land use type layer on the rainfall simulation with the WRF model, the BIAS, MAE and RMSE statistics were applied between the observed rainfall and the simulated rainfall by the WRF model.

The BIAS measures the error that occurs systematically, so it is a good indicator to measure the reliability of the models [28]. It can be positive (overestimation) or negative (underestimation) (Eq. 6):

$$BIAS = \sum_{i=1}^{N} \frac{(P_i - O_i)}{N}, \qquad (6)$$

where N is the number of observations, P_i is the value of the model prediction in element i and O_i is the value of the observation in element i.

The Mean Absolute Error (MAE) is a widely used measure in model evaluations [2, 32]. Provides the average of the absolute difference

between the model prediction and the observed value (Eq. 7):

$$MAE = \frac{\sum_{i=1}^{N} |P_i - O_i|}{N}. \qquad (7)$$

The Root Mean Square Error (RMSE) expresses the total error of the model [32]. Consists of the square root of the sum of the squared errors, which captures both positive and negative errors; therefore, it expresses both systematic and random errors (Eq. 8):

$$RMSE = \sqrt{\sum_{i=1}^{N} \frac{(P_i - O_i)^2}{N}}. \qquad (8)$$

3 Results

Significant variations were observed mainly in the category's farmland and urban zone. Farmland in MODIS classification is minimal, this is considered wrong, since according to INEGI [12], the area for agriculture in the ZMVM amounts to 36%.

It should be considered that urban agriculture is not only within the city, but also on its edges, which have lost their agricultural tradition due to urban expansion. Urban agriculture in these areas is the
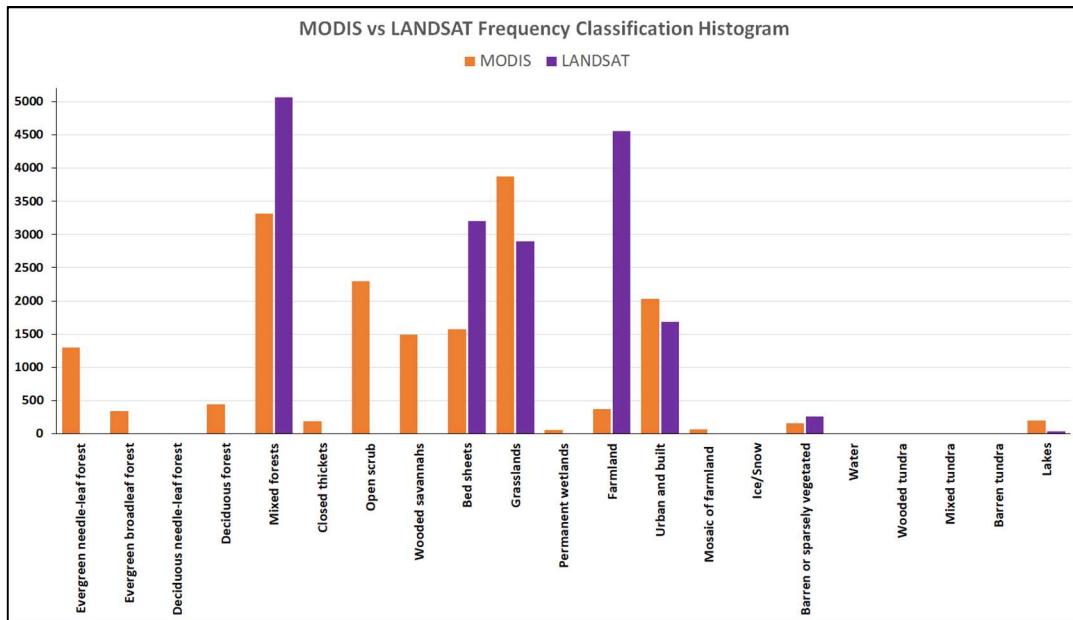
Fig. 4. MODIS and LANDSAT classification frequency histograms

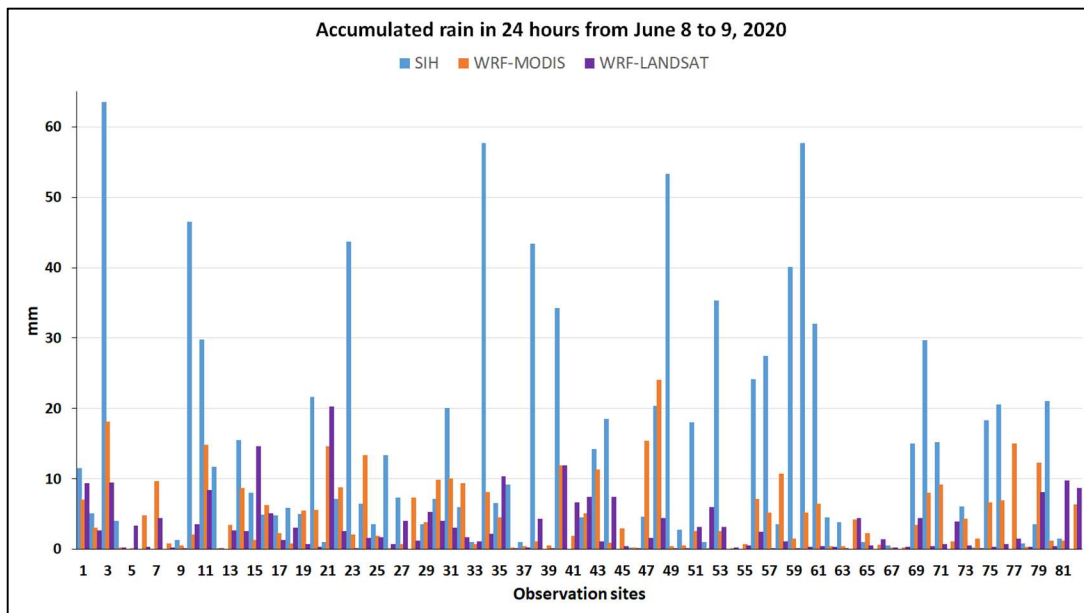**Fig. 5.** Accumulated rainfall (mm) in 24 hours observed, simulated WRF-MODIS and simulated WRF-LANDSAT

result of rural-urban migration, it is a practice that is recovered by the emigrated population with strong community roots towards their places of origin [19].

Regarding the urban zone, the LANDSAT classification detects urban growth in the north and northwest between the limits of the ZMVM and the state of Hidalgo.

However, in MODIS other classifications are considered as urban, therefore in km^2 it presents a higher frequency.

Figure 3 shows the comparison between the MODIS and LANDSAT classification. Figure 4 shows the histogram of frequencies with both classifications. Figure 5 shows the comparison between the rainfall records from the SIH weather stations and those simulated by the WRF model with MODIS and LANDSAT.

Finally, the statistical metrics were applied between the observed values and those simulated by the WRF model for the two simulations. In all the experiments negative BIAS values were obtained, this indicates that the model presents a systematic error with a tendency to underestimate, that is, at the comparison grid points, the model simulates less rainfall than what actually occurred in the ZMVM.

Regarding the MAE metric, this tells us that the expected average error ranges between 10.81 and 11.77 mm. On the other hand, RMSE presents a cumulative variance between 163.56 and 168.09.

However, according to the BIAS, MAE and RMSE metrics, an improvement was observed in the precipitation simulation with the LANSAT classification with respect to MODIS. Table 5 presents the results obtained with the statistical metrics.

4 Conclusions

The methodology presented allowed a classification of the types of land use predominant in the Metropolitan Zone of the Valley of Mexico. Each category can be obtained directly based on the spectral signature of the bands and the derived indices. It was identified that the NDVI can be used as the first classification filter, but not as a determinant, since some land use, such as arid soil, urban areas and farmland present values in the same range, for these cases other indices and auxiliary bands should be used.

The main variation with the updating of the type of land use corresponds to the categories of urban zone and farmland in the Metropolitan Area of the Valley of Mexico. Although the MODIS classification mostly covers Mexico City, it omits some urban spots in the north and northwest that

Table 5. Statistical results for the storm reported by the SIH for June 9, 2020

Metrics	WRF-MODIS	WRF-LANDSAT
BIAS	-9.36	-8.84
MAE	11.77	10.81
RMSE	168.09	163.56

are identified in the LANDSAT classification. Regarding farmland, in the MODIS classification this is minimal, while the LANDSAT classification is considered more realistic. The substitution of the land use type layer on the original file generated by the WRF preprocessing module was transparent, so the numerical simulations were carried out successfully.

The effect on the simulation of the rainfall variable was evaluated for the storm reported by the SIH on June 9, 2020. With a maximum record of 63.5 mm at the "Las arboledas" station with ARBMX code, latitude 19.5667, longitude -99.2167 and an elevation of 2,280 masl. In general, it was observed that the model had a tendency to underestimate, however, there was an improvement in the precipitation simulation with the LANDSAT classification, this based on the statistical results that went from 9.36, 11.77 and 168.09 to -8.84, 10.81 and 163.56 of the BIAS, MAE and RMSE metrics respectively.

The variation in the rainfall simulation with and without updating the land use type layer highlights the sensitivity of the WRF model to the characteristics of the terrain.

Acknowledgments

References

1. **Ariza, A., Roa, O. J., Serrato, P. K. León, H. A. (2017).** Uso de índices espectrales derivados de sensores remotos para la caracterización geomorfológica en zonas

insulares del Caribe colombiano. Revista Perspectiva Geográfica, Vol. 23, No. 1, pp. 105-122. DOI: 10.19053/01233769.5863.

2. **Chai, T., Draxler, R. R. (2014).** Root mean square error (RMSE) or mean absolute error (MAE)? Arguments against avoiding RMSE in the literatura. Geoscientific Model Development, Vol. 7, No. 3, pp. 1247–1250. DOI: 10.5194/gmd-7-1247-2014.

3. **Chen, S. H., Sun, W. Y. (2002).** A one-dimensional time dependent cloud model. Journal of the Meteorological Society of Japan, Vol. 80, No. 1, pp. 99–118.

4. **Chen, F., Kusaka, H., Bornstein, R., Ching, J., Grimmond, C. S. B. (2011).** The integrated WRF/urban modeling system: Development, evaluation, and applications to urban environmental problems. International Journal of Climatology, Vol. 31, No. 2, pp. 273–288, DOI: 10.1002/joc.2158.

5. **Chen, X., Zhao, H., Li, P., Yin, Z. (2006).** Remote sensing image-based analysis of the relationship between urban heat island and land use/cover changes. Remote Sensing of Environment, Vol. 104, No. 2, pp. 133–146. DOI: 10.1016/j.rse.2005.11.016.

6. **Dudhia, J. (1996).** A multi-layer soil temperature model for MM5. The Sixth PSU/NCAR Mesoscale Model Users' Workshop, Boulder, pp. 49–50.

7. **Friedl, M. A., Sulla-Menashe, D., Tan, B., Schneider, A., Ramankutty, N., Sibley, A. Huang, X. (2010).** MODIS collection 5 global land cover: Algorithm refinements and characterization of new datasets. Remote Sensing of Environment, Vol. 114, No. 1, pp. 168–182. DOI: 10.1016/j.rse.2009.08.016.

8. **Garzón, J. E. (2014).** Análisis del efecto de la modificación de la geodatabase (uso del suelo, elevación) en el clima simulado por weather research and forecasting WRF para la Sabana de Bogotá. Tesis de licenciatura. Universidad Nacional de Colombia.

9. **Grell, G. A., Freitas, S. R. (2014).** A scale and aerosol aware stochastic convective parameterization for weather and air quality modeling. Atmospheric Chemistry and Physics, Vol. 14, pp. 5233–5250. DOI: 10.5194/acp-14-5233-2014.

10. **González-Luna, C., Filonov, A., Mireles, O. Tereshchenko, I. (2019).** Análisis espectral y dispersión superficial de detritos suspendidos en la Bahía de Banderas mediante imágenes de satélite. Revista Cartográfica, Vol. 98, pp. 223-237. DOI: 10.35424/rcarto.i98.148.

11. **Iacono, M. J., Delamere, J. S., Mlawer, E. J., Shephard, M. W., Clough, S. A., Collins, W. D. (2008).** Radiative forcing by long-lived greenhouse gases: Calculations with the AER radiative transfer models. Journal of Geophyssical Research, Vol. 113, No. D13103, pp. 1–8. DOI: 10.1029/2008JD 009944.

12. **Instituto Nacional de Estadística y Geografía (INEGI). (2014).** Cuaderno estadístico y geográfico de la zona metropolitana del Valle de México 2014. INEGI: México.

13. **Jiménez, P. A., Dudhia, J., González–Rouco, F., Navarro, J., Montavez, J. P., Garcia–Bustamante, E. (2012).** A revised scheme for the WRF surface layer formulation. Monthly Weather Review, Vol. 140, No. 3, pp. 898–918. DOI: 10.1175/MWR-D-11-00056.1.

14. **Kawamura, M., Jayamana, S., Tsujiko, Y. (1996).** Relation between social and environmental conditions in Colombo Sri Lanka and the urban index estimated by satellite remote sensing data. The International Archives of Photogrammetry and Remote Sensing, Vol. 31, pp. 321–326.

15. **Milbrandt, J. A., Yau, M. K. (2005a).** A multimoment bulk microphysics parameterization. Part I: Analysis of the role of the spectral shape parameter. Journal of Atmospheric Science, Vol. 62, No. 9, pp. 3051–3064. DOI: 10.1175/JAS3534.1.

16. **Milbrandt, J. A., Yau, M. K. (2005b).** A multimoment bulk microphysics parameterization. Part II: A proposed three–moment closure and scheme description. Journal of Atmospheric Science, Vol. 62, No. 9, pp. 3065–308. DOI: 10.1175/JAS3535.1.

17. **Mireles, I. O., Filonov, A., González, C. A., Tereshchenko, I. (2019).** La percepción

remota en el seguimiento de plumas de detritos en bahía de banderas, Jalisco-Nayarit, México. Revista Internacional de Contaminación Ambiental, Vol. 35, No. 3, pp. 671–681, DOI: 10.20937/RICA.2019.35.03.12.

18. **Morales, L. G. (2019).** Uso del modelo WRF para monitoreo de huracanes en México .Instituto Politécnico Nacional, ESIA, Tesis de licenciatura, pp. 1–96.

19. **Moreno-Gaytán, S. I., Jiménez-Velázquez, M. A., Hernández-Juárez, M. (2019).** Sustentabilidad y agricultura urbana practicada por mujeres en la Zona Metropolitana de Ciudad de México, Valle de Chalco Solidaridad. Revista de Alimentación Contemporánea y Desarrollo Regional, Vol. 29, No. 54, pp. 2–33. DOI: 10.24836/es.v29i54.795.

20. **Muñoz, R., Radic, S. (2015**). Uso de percepción remota y SIG en la selección de sitios de muestreo de suelos para la región de Magallanes. Agro Sur, Vol. 43, No. 2, pp. 65–76. DOI: 10.4206/agrosur.2015.v43n2-08.

21. **Nakanishi, M., Niino, H. (2006).** An improved Mellor–Yamada level 3 model: Its numerical stability and application to a regional prediction of advecting fog. Boundary Layer Meteorology, Vol. 119, pp. 397–407. DOI: 10.1007/s10546-005-9030-8.

22. **Nakanishi, M., Niino, H. (2009).** Development of an improved turbulence closure model for the atmospheric boundary layer. Journal of the Meteorological Society of Japan, Vol. 87, No. 5, pp. 895–912. DOI: 10.2151/jmsj.87.895.

23. **National Center for Atmospheric Research (NCAR).** (**2022).** The weather research & forecasting model. mesoescale & microescale meteorology laboratory. https://www.mmm.ucar.edu/weather-research andforecasting-model

24. **National Centers for Environmental Prediction (NCEP) (2021).** NCEP FNL Operational model global tropospheric analyses, continuing from July 1999. NCEP: USA.

25. **Olson, J. B., Kenyon, J, Wayne, A., Brown, J., Pagowski, M., Sušelj, K. (2019).** A Description of the MYNN-EDMF scheme and the coupling to other components in WRF–ARW. NOAA Technical Memorandum OAR GSD 61, USA. DOI: 10.25923/n9wm-be49.

26. **Organization for Economic Cooperation and Development (OECD), (2015).** OECD Territorial Reviews: Valle de México, México. OECD Library: USA.

27. **Perilla, G., Mas, J. F. (2020).** Google Earth Engine: Una poderosa herramienta que vincula el potencial de los datos masivos y la eficacia del procesamiento en la nube. Investigaciones Geográficas, Vol. 101, pp. 1–6. DOI: 10.14350/rig.59929.

28. **Ravinder, H. V. (2017).** Bias in aggregations of subjective probability and utility. Journal of the Operational Research Society, Vol. 43, No. 6, pp. 621–627, DOI: 10.1057/jors.1992.87.

29. **Sanz, E., Saa-Requejo, A., Díaz-Hambrona, C. H., Ruiz-Ramos, M., Rodríguez, A., Iglesias, E., Esteve, P., Soriano, B., Tarquis, A. M. (2021).** Normalized difference vegetation index temporal responses to temperature and precipitation in arid rangelands. Remote Sensing, Vol. 13, No. 5, pp. 1–24. DOI: 10.3390/rs13050840.

30. **Secretaría del Medio Ambiente del Gobierno de la Ciudad de México (SEDEMA), Secretaría de Medio Ambiente y Recursos Naturales (SEMARNAT), Secretaría del Medio Ambiente del Gobierno del Estado de México (SMAGEM) & Secretaría de Medio Ambiente y Recursos Naturales del Gobierno del Estado de Hidalgo (SEMARNATH) (2021).** Programa de gestión para mejorar la calidad del aire de la zona metropolitana del Valle de México (ProAire ZMVM 2021-2030). SEDEMA, SEMARTNAT, SMAGEM & SEMARNATH: Ciudad de México.

31. **Skamarock, W. C., Klemp, J. B., Dudhia, J., Gill, D. O., Liu, Z., Berner, J., Wang, W., Powers, J. G., Duda, M. G., Barker, D. M., Huang, X. Y. (2019).** A description of the advanced research WRF version 4. NCAR Technical Note NCAR/TN-556+STR: USA.

32. **Souza, N. B. P., Nascimento, E. G. S., Moreira, D. M. (2023).** Performance evaluation of the WRF model in a tropical

region: Wind speed analysis at different sites. Atmósfera, Vol. 36, No. 2, pp. 253–277. DOI: 10.20937/ATM.52968.

33. **Thompson, J. B., Zurita-Arthos, L., Müller, F., Chimbolema, S., Suárez, E. (2021).** Land use change in the Ecuadorian páramo: The impact of expanding agriculture on soil carbon storage. Arctic, Antarctic, and Alpine Research, Vol. 53, No. 1, pp. 48–59. DOI: 10.1080/15230430.2021.1873055.

34. **Veneros, J., García, L., Morales, E., Gómez, V., Torres, M., López, F. (2020).** Aplicación de sensores remotos para el análisis de cobertura vegetal y cuerpos de agua. IDESIA, Vol. 38, No. 4, pp. 99–107. DOI: 0.4067/S0718-34292020000400099.

35. **Zha, Y., Gao, J., NI, S**. (2003). Use of normalized difference built-up index in automatically mapping urban from TM imagery. International Journal of Remote Sensing, Vol. 24, No. 3, pp. 583–594. DOI: 10.1080/01431160304987.